Wideband RCS reduction based on a simple chessboard metasurface

Zhou, Changfei; Yu, Qi Feng; Gustafson, Carl; Lau, Buon Kiong

Published in:
Journal of Applied Physics

DOI:
10.1063/5.0143001

2023

Document Version:
Peer reviewed version (aka post-print)

Journal of Applied Physics

AIP Publishing

Wideband RCS Reduction Based on a Simple Chessboard Metasurface

C. F. ZHOU[1], Q. F. YU[1], C. GUSTAFSON[2] AND B. K. LAU[3]

[1] *School of Information and Communication Engineering, Dalian University of Technology, Dalian, 116024, China.*
[2]*SAAB Dynamics, Linköping, 58188, Sweden.*
[3]*Department of Electrical and Information Technology, Lund University, Lund, 221 00, Sweden.*
**cfzhou@dlut.edu.cn*

Abstract: To avoid being detected by radar, it is necessary to reduce stealthy military platforms' radar cross section (RCS). The operation of overlaying the metasurface on the targets is a good solution. A simple chessboard MS structure that can achieve low RCS over a large bandwidth is proposed. Only one unit cell is used to construct the MS. First, the unit cell working in 0.5 and 1-λ modes is designed to achieve a stable phase difference of 180° for *y*- and *x*-polarized waves. Then, the unit cells and rotated ones are used to form a chessboard structure with different distributions. The compared results show that the chessboard MS with 2 × 2 quadrants can facilitate the widest 10 dB RCS reduction band of 111% and the largest RCS reduction. The proposed structure exhibits excellent RCS reduction even when irradiated by *y*- and *x*-polarized waves at an oblique incidence of 30°.

1. Introduction

Techniques for reducing radar cross section (RCS) are in high demand for military equipment that requires stealth operation. Due to the flexible electromagnetic (EM) wave control capability [1-4] and low profile [5-7], metasurface (MS) has gained tremendous attention in recent research into RCS reduction.

In particular, absorptive MS is a popular technique to reduce RCS [8-11]. When an incident wave illuminates the absorber, the EM energy will be converted into heat, resulting in a low reflected EM wave energy. However, each element of the absorptive MS array requires several resistors, which increases the weight, cost, and fabrication complexity. For non-absorptive MS, RCS reduction is based on the cancellation of the scattering by the MS [12-20], e.g., between two elements giving equal amplitude and out-of-phase scattered waves. This kind of MS is lightweight since no resistor is needed. In [12], an artificial magnetic conductor (AMC) and perfect electric conductor (PEC) with 0° and 180° reflection phases, respectively, were combined to realize RCS reduction. To broaden the 10 dB RCS reduction bandwidth, two AMC elements (1-bit) were investigated to maintain the required phase difference of 180°±37° [13-15]. Most of these scattering-cancellation based MSs adopt a chessboard arrangement [16-21]. Among [16-21], the reflected phases of different elements were mainly adjusted by the dimensions of the unit cell or the element shape. However, different unit cells (more than two) were required to compose the MS, which increased the design complexity. Recently, polarization conversion metasurface (PCM) is used to reduce RCS [3, 22-26], because a perfect phase difference of 180° is generated between the polarization converter and its mirror structure for the same incident wave. In addition, using two units of different heights to achieve a phase difference of 180° ± 37° with the help of height difference is also a novel approach [27]. When the MS elements are designed with the desired reflected wave phases, the RCS reduction performance is primarily dependent on the distribution of the unit cells. Recently, optimization algorithms [15, 28-33], such as genetic algorithm and particle swarm optimization (PSO) algorithm, are used to optimize the RCS reduction performance. However, the optimization

algorithms are time-consuming and increase the design complexity. Therefore, it is highly desirable to achieve high RCS reduction with a simple MS structure that can be designed easily. As a result, the chessboard structure is widely used because of its easy design principle [16-21]. Nevertheless, even with this structure, the internal distributions of the chessboard elements can largely influence the final RCS performance [19].

In this paper, a simple MS structure that can achieve low RCS over a large bandwidth is proposed. First, a unit cell is designed to achieve a phase difference of 180°±37° within a wide band for the *y* and *x*-polarized waves. Then, the proposed unit cells are grouped to compare the effect of different chessboard distributions on the RCS reduction of the MS. By comparing the 6 × 6, 4 × 4, 3 × 3, and 2 × 2 elements distributions, it is found that the 2 × 2 case yields the widest 10 dB RCS reduction band of 111% as well as large RCS reduction values. To demonstrate the oblique incidence capability of the proposed structure, 30° and 45° oblique incidences are simulated. The proposed structure exhibits excellent RCS reduction even when irradiated by *y*- and *x*-polarized waves at an oblique incidence of 30°.

2. Design of Metasurface

2.1 Unit cell

The unit cell in the proposed MS array is shown in Figure 1, consisting of two-layer dielectric substrates. The upper layer is a pure dielectric block without any printed metal. A metal strip is printed on the top surface of the lower substrate layer, and the metal ground is printed on the back surface of the lower substrate layer. Both the upper and lower substrate layers are made of RO4725JXR material, with a relative permittivity of 2.55 and a loss tangent of 0.0022. The unit cell is designed to generate a 180° phase difference between the *y* and *x* polarized incident waves. The final optimized dimensions of the unit cell are shown in Table 1.

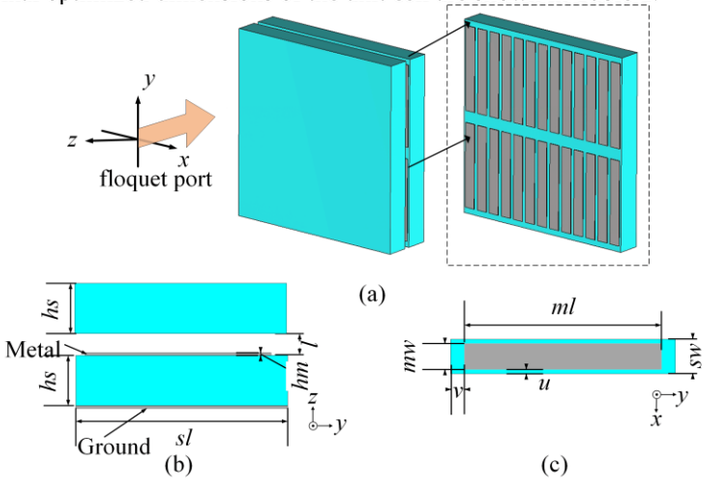

Fig. 1. (a) Schematic illustration of the unit cells in the array. (b) Side view of a unit cell. (c) Top view of a unit cell without the upper substrate layer.

Table 1. Parametric values of the proposed unit cell (mm)

hs	*hm*	*sl*	*l*	*mw*
1.5	0.018	6.5	0.4	0.75
ml	*sw*	*u*	*v*	
5.7	1	0.125	0.4	

2.2 Unit cell performance study

The proposed unit cell is designed and studied with the frequency domain solver of the EM simulation tool CST 2021. The boundary conditions of the cell are set to be unit cell in the *x* and *y* directions, electric (E_t=0) in the -*z* direction, and open (add space) in the +*z* direction. The simulated port is set to Floquet port. In the simulation, *y*- and *x*-polarized incident waves illuminate the MS with infinite periodic elements. Due to the large length-width ratio of the element, different reflection phases are generated, which are shown in Figure 2. It can be seen that the unit cell can achieve a phase difference of 180°±37° in the range of 9.3-30.6 GHz (21.3 GHz, 107%). Figure 2 shows reflection amplitude is close to 0 dB in the whole frequency band.

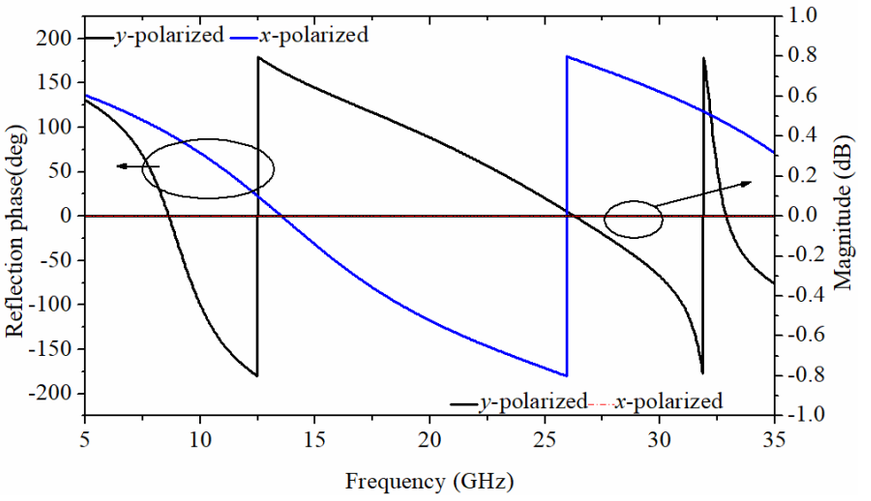

Fig. 2. The reflection phase and amplitude of the unit cell with *y*- and *x*-polarized incident waves.

The surface current distributions of the unit cell are simulated with periodic boundary conditions to analyze its operating modes at different frequencies. Figure 3 shows the current distribution on the top surface (metal strip) and the back surface (ground) of the lower substrate layer at 9, 15.5, and 31 GHz. The current plotted in Figure 3(a) is consistent with a magnetic resonance producing a current loop having conductive current in the top patterned metal and the ground plane in opposite direction and a displacement current between them. With a weak current on the ground, the current plotted in Figure 3(b) at 15.5 GHz is a resonance of the metallic strip with a matching condition of the strip length with half a wavelength. To sum up, the two resonances are produced by a magnetic field in *x* direction for the first resonance and by an electric field in *y* direction for the second one. Finally, the current plot in Figure 3(c) works as a second order magnetic resonance with one waveguide wavelength.

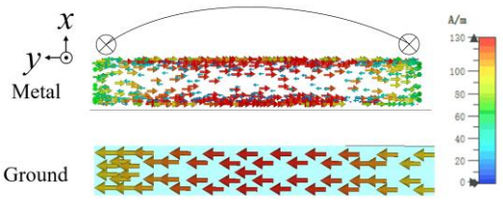

(a)

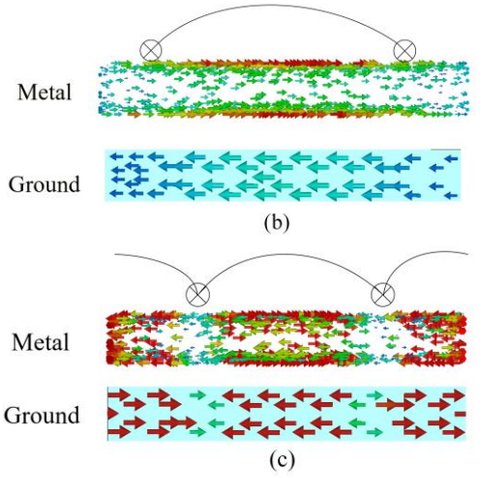

Fig. 3. At different frequencies, the current distribution on the metal strip and the ground surface when the *y*-polarized wave is incident: (a) 9 GHz, (b) 15.5 GHz, (c) 31 GHz.

The length-width ratio is the main parameter to generate the 180° phase difference between the *y* and *x*-polarized waves. Thus, the length-width ratio of the unit cell is parametrically studied in Figure 4. It is noted that the gaps between the edges of the metal strip and the dielectric plate affect the reflection phase of the unit cell. Therefore, to facilitate fair comparison, they are kept constant at u = 0.125 mm and v = 0.4 mm for different length-width ratios (sl/sw). It is observed that when the length-width ratio is equal to 6.5, a larger bandwidth can be obtained to satisfy the requirement of 180°±37° phase difference.

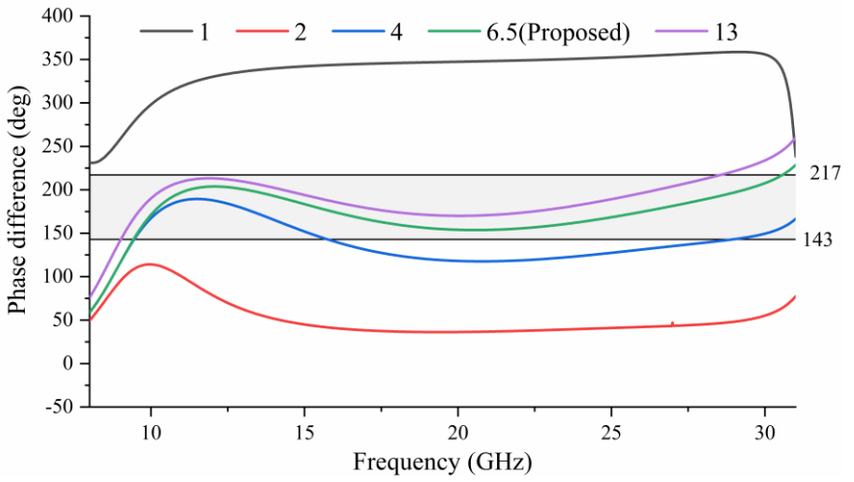

Fig. 4. Reflection phase difference of unit cells with different length-width ratios.

To balance the RCS reduction performance of the array with the smallest thickness, the air gap l is scanned parametrically. The phase difference results are shown in Figure 5. It can be seen that l=0.4 and l=0.6 have a more stable phase difference. To reduce the overall thickness l=0.4 is chosen.

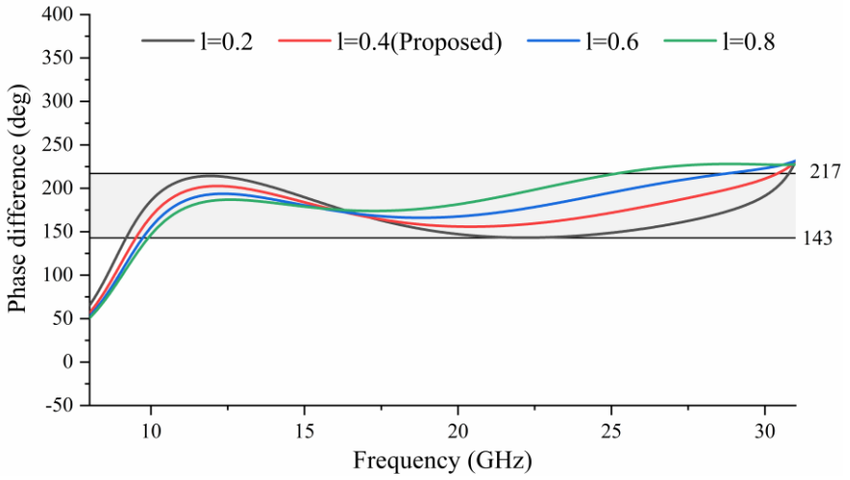

Fig. 5. The reflection phase difference of unit cells with different air gaps.

To show the effect of the upper substrate layer, the unit cell without the upper substrate layer is compared in Figure 6. It can be seen that the upper substrate layer facilitates a stable phase difference of 180°±37°, thereby broadening the bandwidth.

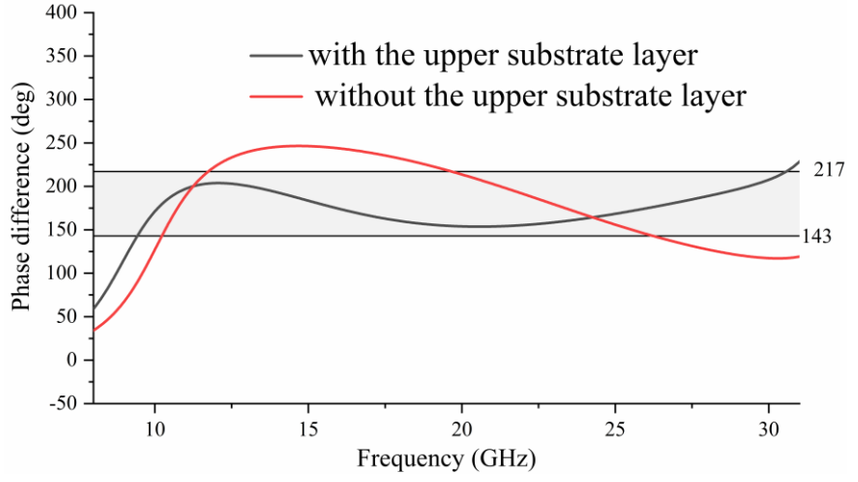

Fig. 6. Reflection phase difference of the element with / without the upper substrate layer.

To explain the working mechanism of the function of the upper substrate, two groups of simulations have been done in Figure 7. The reflection phases of the unit cell with and without the upper substrate are shown in Figure 7(a) and (b), and the reflection phases of the unit cell with different thicknesses of the upper substrate are also shown in Figure 7(c) and (d). It can be found that the slope of the *y*- and *x*-polarized incidence with the upper substrate is larger than that without the upper substrate. The thicker the upper substrate, the greater the slope of the *y* polarized. The cause of this phenomenon can be thought of as adding an upper layer of dielectric increases the effective permittivity around the resonator, making the resonant frequency lower and thus causing the phase slope to be increased. By adding the upper substrate

layer and choosing a suitable thickness, the slope of the *y*-polarized wave reflection phase is successfully made closer to the *x*-polarized wave reflection phase slope, maintaining the stability of the phase difference of 180°.

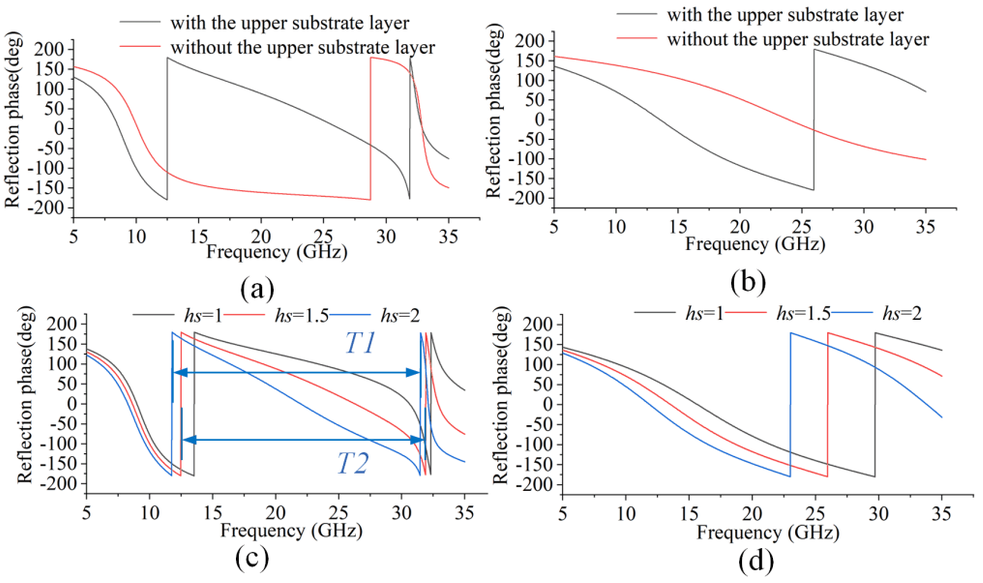

Fig. 7. Reflection phase of the unit cell with and without the upper substrate of (a) *y* and (b) *x* polarized incident wave, reflection phase of the unit cell with different heights of (c) *y* and (d) *x* polarized incident wave.

2.3 Arrangement of MS

The *y*-polarized wave and *x*-polarized wave in broadside direction are rotated by 90°, which means that the reflected phase of the *x* polarized wave in Figure 2 is the reflected phase of the *y*-polarized wave after rotating the unit by 90°. Based on the 180° phase difference of *y* and *x*-polarized wave in Figure 2, the phase of the original unit cell and the 90° rotated version of the unit cell will cancel when illuminated by the *y*(*x*) polarized wave, thus reducing the reflection. The unit cells and the rotated ones are used to construct the chessboard. The monostatic RCS can be calculated by equations (1) and (2) [13]:

$$\vec{E}_r = A_1 e^{j\varphi_1} \cdot AF_1 + A_2 e^{j\varphi_2} \cdot AF_2 \tag{1}$$

$$RCS \text{ reduction} = 10\log\left(\frac{\left|A_1 e^{j\varphi_1} + A_2 e^{j\varphi_2}\right|^2}{\left|\vec{E}_r^{\,\mathrm{PEC}}\right|^2}\right) \tag{2}$$

where A_1 and φ_1 are the reflected amplitude and phase of the original unit cell. A_2 and φ_2 are the reflected amplitude and phase of the unit cell after 90° rotation. $AF_1 = e^{-j\pi d\cos\phi/\lambda}$ and $AF_2 = e^{j\pi d\cos\phi/\lambda}$ are the array factors of the two scatters, where ϕ represents reflection direction and λ represents the wavelength of the incident waves. $\left|\vec{E}_r^{\,\mathrm{PEC}}\right|$ is the reflected E-field of the PEC plate. At 0° incidence, $AF_1 = AF_2 = 1$.For lossless scatters, $|A_1| = |A_2| = 1$. Thus, when $\varphi_1 - \varphi_2 = 180^\circ$, ultralow RCS can be achieved. If the RCS reduction is over 10 dB,

$\left|A_1 e^{j\varphi_1} + A_2 e^{j\varphi_2}\right| \leq 0.632$ is needed [13], that is, the reflected phase difference of two scatters should be within the range of 180°±37°.

To find the best chessboard structure of the MS to achieve the lowest RCS, the unit cells are arrayed in 4 rows, 6 rows, 8 rows, and 12 rows to construct the MS with 6 × 6, 4 × 4, 3 × 3, and 2 × 2 matrix elements, respectively, as shown in Figure 8. The boundary between the matrix element and the rotated one is not continuous, which affects the MS performance. For example, apart from the outer boundary common to both 4 × 4 and 2 × 2 configurations, fewer matrix elements experience the boundary effect for the 2 × 2 elements than for the 4 × 4 elements. In all configurations, the number of unit cells are the same. This also means that more matrix elements in the 4 × 4 case deviate from the designed performance relative to the 2 × 2 case, resulting in its poorer RCS performance. Thus, the best performance of phase cancellation can be achieved by the proposed MS. The monostatic RCS reduction of the four chessboard structures compared with an all-metal plate of the same size is shown in Figure 9. The 10 dB RCS reduction bandwidths of the four kinds of arrays are obtained in Table 2. It can be seen that the relative bandwidth of the array with 2 × 2 matrix elements is the largest, which provides the best overall RCS reduction. It achieves a bandwidth of 111%, with two deep RCS reductions of -37.5 dB at 10 GHz and -39.7dB at 27 GHz. Thus, for the chessboard MS structure, the unit cells should be distributed within 2×2 matrix elements to obtain the best RCS reduction performance.

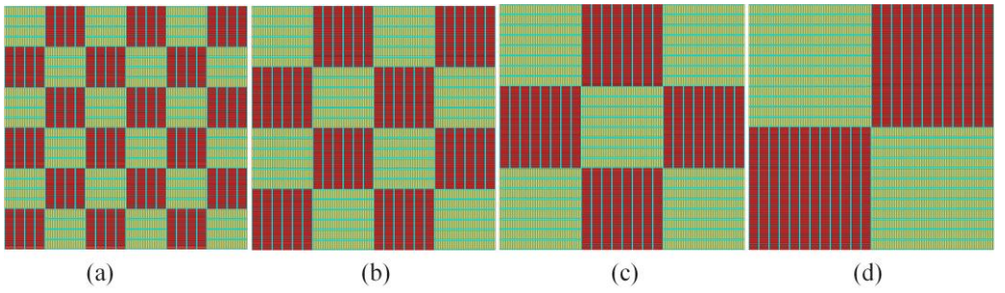

Fig. 8. (a) 6 × 6, (b) 4 × 4, (c) 3 × 3, (d) 2 × 2 matrix elements

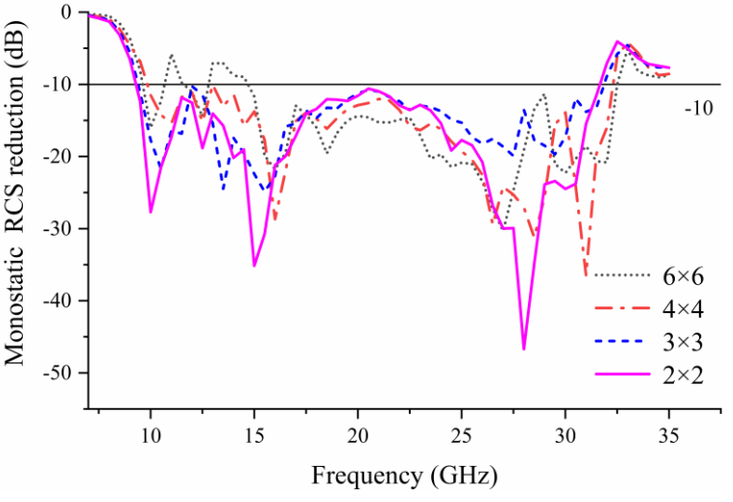

Fig. 9. The RCS reduction of four chessboard structures.

Table 2. The 10dB RCS reduction bandwidth and relative bandwidth of four kinds of arrays.

matrix elements	10dB RCS reduced bandwidth (GHz)	relative bandwidth
6 × 6	9.5-10.7、11.5-12.9、14.5-32.5	100%
4 × 4	9.54-32.4	109%
3 × 3	9.33-32	110%
2 × 2	9.1-31.7	111%

To show the RCS reduction performance more intuitively, the simulated 3D scattering pattern of the chessboard MS (2 × 2 matrix elements) at 9.5 GHz, 16 GHz, 23 GHz and 31 GHz are given in Figure 10. The time domain solver is used to obtain the RCS of the whole chessboard MS, and the boundary conditions are set to be open (add space) and wave source is set to be plane wave in CST for the simulation. It is worth noting that although the scattering pattern of the *x*-polarized plane wave is presented here, the *y*-polarized plane wave also has the same scattering pattern because of the 0° incidence. It is observed that the scattering pattern of the MS owns four oblique lobes, and the broadside radiation becomes a null due to the cancellation, leading to a good monostatic RCS reduction. Compared with the PEC, the proposed scattering pattern exhibits smaller amplitude around the broadside direction. The incident wave will be evenly scattered after being reflected by the MS, achieving the purpose of reducing RCS.

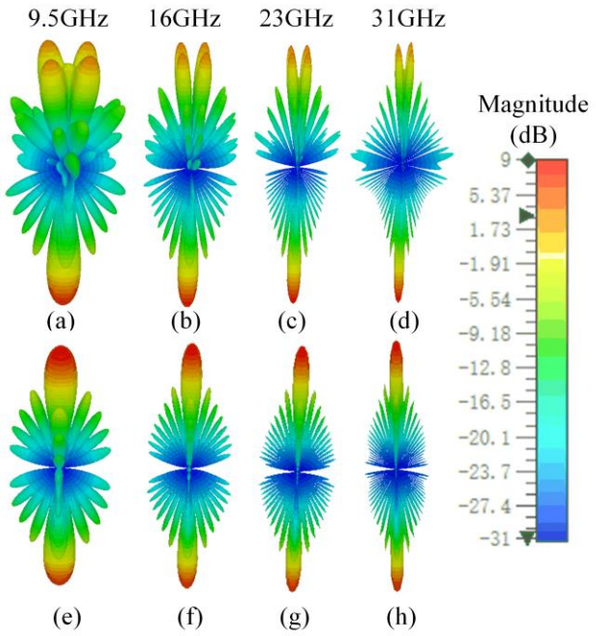

Fig. 10. 3-D scattering patterns at different frequency under *x*-polarized plane wave at (a) 9.5 GHz, (b) 16 GHz,(c) 23 GHz, (d) 31 GHz of the proposed MS, (e) 9.5 GHz, (f) 16 GHz, (g) 23 GHz, (h) 31 GHz of the PEC.

The 2D monostatic RCS plots of the proposed MS are shown in Figure 11. It can be seen that the reflected waves are scattered in four directions and the reflected waves are weak in the broadside direction. Simulated results show that the difference between the co- and cross-polarized RCS is larger than 30 dB.

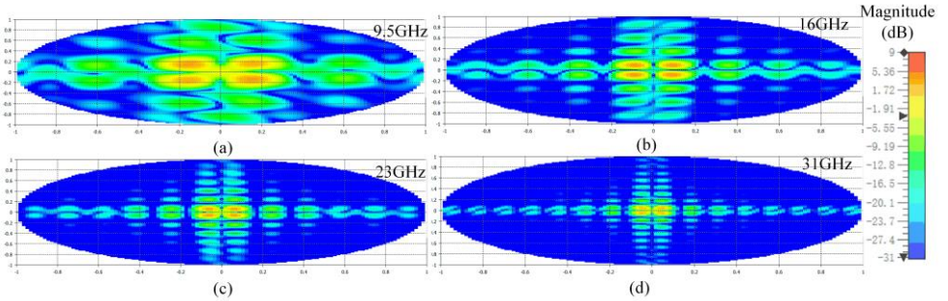

Fig. 11. 2D monostatic RCS under *x*-polarized plane wave at (a) 9.5 GHz, (b) 16 GHz,(c) 23 GHz, (d) 31 GHz of the proposed MS

The proposed checkerboard structure is composed of the original unit cell and its unit cell rotated by 90°. The *y*-polarized and *x*-polarized waves are also related by 90° rotation in the broadside direction. At 0° incidence, the proposed structure has nearly the same scattering ability for *y*-polarized and *x*-polarized waves. For the proposed array, the RCS of *y*-polarized and *x*-polarized waves at 0° incidence is obtained in Figure 12. It can be seen that the two curves match perfectly.

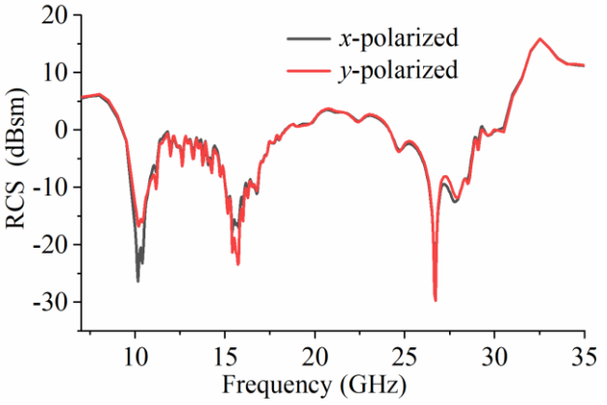

Fig. 12. RCS reduction of the MS of *y*-polarized and *x*-polarized incident waves

To demonstrate the scattering capability of the proposed array at oblique incidence, the RCS reduction at incidence angles of 30° and 45° is simulated as shown in Figure 13. Figure 13 plots the bistatic RCS reduction. Incident wave angle is theta=30°/45°, phi=0°, and the measured reflected wave angle is theta=30°/45°, phi=180°. For *x*-polarized waves, the RCS reduction can be up to -10 dB in the band range of 10-23.3 GHz and 26.1-29 GHz when the plane wave is incident at 30°. When the plane wave is incident at 45°, the RCS reduction can reach -10dB in the band of 10.8-20.8GHz and 22.8-26.3GHz. For *y*-polarized wave, when the plane wave is incident at 30°, the RCS reduction is basically below -10dB in the band of 9.5-31.5GHz. When the plane wave is incident at 45°, the RCS reduction is up to -10dB in the band range of 9.5-10.5GHz and 15.3-31GHz. This structure also has excellent RCS reduction at an oblique incidence of 30°, but the performance reaches its limit at an incidence angle of 45°.

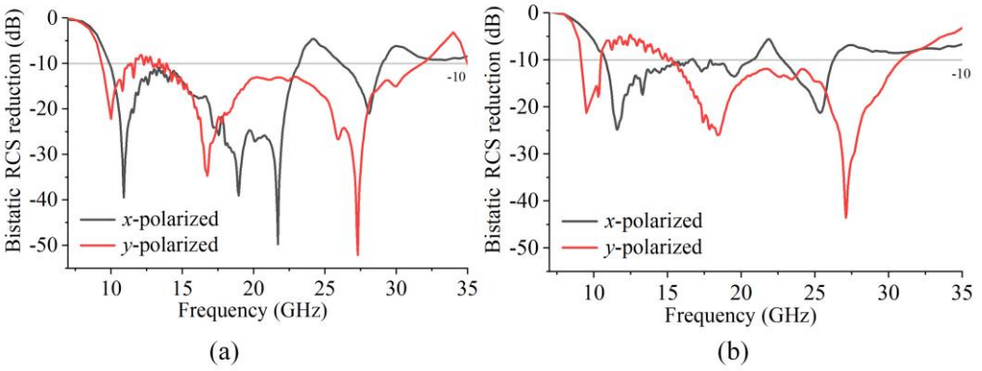

Fig. 13. Bistatic RCS reduction at oblique incidence of (a) 30°. (b) 45°.

3 Measurement and discussion

To verify the simulated results, the chessboard MS with 2×2 matrix elements was fabricated and measured. The fabricated structure is shown in Figure 14, small shims were used to keep the air gap between the upper and lower substrates. A few horn antennas were used to perform monostatic measurement to cover the measured frequency range of 5-37.5 GHz. The horn antennas were mounted at the top of the arc, facing directly down towards the floor. The device under test (DUT) was placed below the antenna on top of a block of styrofoam in the shape of a cuboid. The DUT was measured using a Keysight Vector Network Analyzer, as shown in Figure 14(c). This was done for the front of the proposed MS as well as for the PEC with the same size. The PEC used for measurement is the back plane of the proposed MS, thus, by turning over the MS, the PEC is placed on a styrofoam at the same distance as the input plane of the MS. The RCS curves obtained through simulation and experiment are shown in Figure 15. It is important to note that the test results here are the RCS reduction of the *x*-polarized wave at 0° incidence. At 0° incidence, the proposed structure has nearly the same scattering ability for *y*-polarized and *x*-polarized waves. Thus, only the test results of *x*-polarized wave incidence are given here.

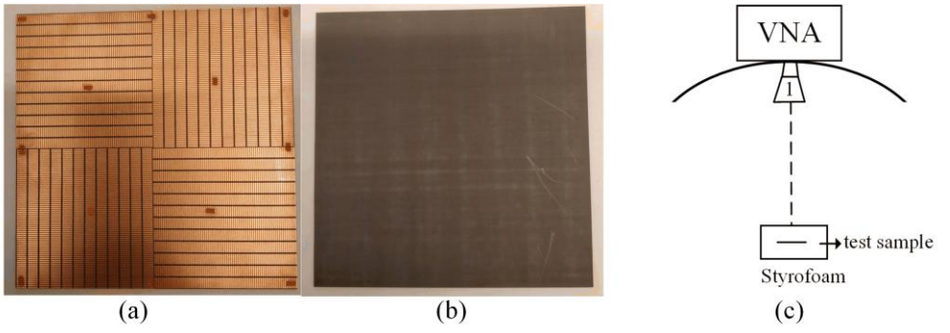

Fig. 14. Structure of the fabrication. (a) Top view without the upper substrate.(b) upper substrate, (c) test environment.

Good agreement can be seen between the measured and simulated results. The error can be summarized in two parts: fabrication and measurement. The air gap between the two dielectric plates is 0.4 mm. Although a 0.4 mm shim is used, errors are inevitable. Since the main lobe of the RCS pattern gets narrower at higher frequencies, the device under test (DUT) has to be

precisely aligned, which should be perpendicular and centered against the measurement antennas to measure the RCS accurately. Because the angular alignment at higher frequency is challenging, the discrepancy gets larger.

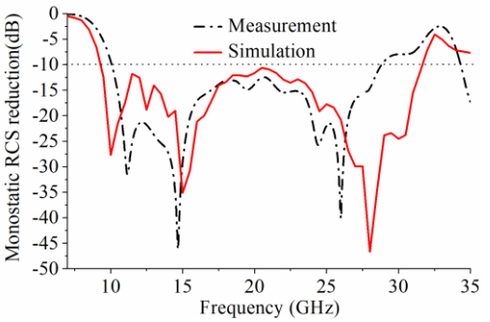

Fig. 15. Simulated and measured RCS results of the MS with 2 × 2 matrix elements.

Based on the above analysis, the steps for designing MS are as follows:
(1) Print the metal strip on the long substrate, place a substrate above the strip, as shown in Figure 1(b).
(2) Tune the length-width ratio of the strip to get the wideband 180° phase difference between the *y*- and *x*-polarized incident waves.
(3) Compose a square unit cell using the strips, as shown in Figure 1(a).
(4) Form a 2 × 2 distributed checkerboard array with the unit cells and the 90° rotated unit cells.
(5) Fabricate the checkerboard MS, and place shims to keep the air gap between the two substrates.

Table 3 provides a comparison between the proposed MS and those proposed by other researchers. It can be concluded that while the structure and design method of the proposed MS are simpler than previous designs, it achieves low RCS over a larger bandwidth.

Table 3. Comparison with Other Works.

Ref.	Method	10 dB RCS reduction bandwidth	Thickness	RO	With resistors	DC	No. of unit cells
[8]	PC+ ABS+ 180° PD	1.85-19.2 (164.8%)	0.11λ	No checkerboard	Yes	High	3
[10]	ABS	5.4-15.7 (97.6%)	0.13λ	No	Yes	Medium	1
[13]	ABS+ 180° PD	4.1-12 (98.9%)	0.12λ	No checkerboard	Yes	Low	2
[19]	180° PD	3.76-7.51 (67%)	0.08λ	No checkerboard	No	Low	2
[20]	180° PD	3.94-7.40 (61%), 8.41-10.72 (24%)	0.08λ	No checkerboard	No	Medium	2
[25]	PC+ 180° PD	7.5-22.5 (100%)	0.075λ	Yes	No	High	32
[28]	PC+ 180° PD	9.26-12.87 (32.6%), 14.84-19.35 (26.4%)	0.09λ	Yes	No	Medium	1
[29]	180° PD	15-35 (80%)	0.08λ	Yes	No	High	1
[30]	PC+ 180° PD	5.21-15.09 (97.3%)	0.07λ	Yes	No	Medium	2
This work	180° PD	9.1-31.7 (111%)	0.11λ	No checkerboard	No	Low	1

PD: phase difference. PC: polarization conversion. ABS: absorptive material. RO: requiring optimization. DC: design complexity. λ is calculated based on the lowest frequency.

4. Conclusions

In this paper, a novel unit cell is designed to achieve a phase difference of 180°±37° for *y*- and *x*-polarized wave within 9.3-30.6 GHz, working in 0.5 and 1-λ modes. Different distributions of the chessboard MS are compared, and the 2 × 2 quadrants array provides the best performance, with the 10 dB RCS reduction bandwidth of 9.1 GHz-31.7 GHz (111%, *x*-polarized wave 0° incidence). The proposed structure exhibits excellent RCS reduction even when irradiated by *y*- and *x*-polarized waves at an oblique incidence of 30°. The proposed MS exhibits the characteristics of simple structure, wideband and low RCS, and only one unit cell is needed to construct the chessboard MS.

Acknowledgments

We would like to thank A. Johansson and M. Nilsson for their help in fabricating the prototype.

References

1 D. R. Yang, Y.Z. Cheng, F. Chen, H. Luo, L. Wu, "Efficiency tunable broadband terahertz graphene metasurface for circular polarization anomalous reflection and plane focusing effect," Diam Relat Mater. 131,109605 (2023)
2 E. Y. Zhou, Y. Z. Cheng, F. Chen, H. Luo, "Wideband and high-gain patch antenna with reflective focusing metasurface," Int J Electron Commun. 134.153709 (2021)
3 J. P. Fan, Y. Z. Cheng, "Broadband high-efficiency cross-polarization conversion and multi-functional wavefront manipulation based on chiral structure metasurface for terahertz wave," J. Phys. D. 53. 025109 (2020)
4 J. P. Fan, Y. Z. Cheng, B. He, "High-efficiency ultrathin terahertz geometric metasurface for full-space wavefront manipulation at two frequencies" J. Phys. D. 54. 115101 (2021)
5 C. Huang, C. L. Zhang, J. N. Yang, B. Sun, X. G. Luo, "Reconfigurable metasurface for multifunctional control of electromagnetic waves," Adv. Opt. Mater. 5, 1700485 (2017)
6 Q. W. Lin, H. Wong, L. Huitema, A. Crunteanu, "Coding metasurfaces with reconfiguration capabilities based on optical activation of Phase-Change materials for terahertz beam manipulations," Adv. Opt. Mater. 10,.2101699 (2022)
7 K. Chen, N. Zhang, G. W. Ding, J. M. Zhao, T. Jing, Y. J. Feng, "Active anisotropic coding metasurface with independent real-time reconfigurability for dual polarized waves," Adv. Mater. Technol. 5, 1800930 (2019)
8 L. Zhou, Z. X. Shen, "Absorptive coding metasurface with ultrawideband backscattering reduction," IEEE Antennas Wireless Propag Lett. 19, 1201-1205(2020)
9 X. Begaud, A. C. Lepage, S. Varault, M. Soiron, A. Barka, "Ultra-wideband and wide-angle microwave metamaterial absorber," Materials. 11, 1-9(2018)
10 Q. Chen, M. Guo, D. Sang, Z. Sun, Y. Fu, "RCS reduction of patch array antenna using anisotropic resistive metasurface," IEEE Antennas Wireless Propag Lett. 18, 1223-1227(2019)
11 J. Wang, R. Yang, R. Ma, J. Tian, W. Zhang, "Reconfigurable multifunctional metasurface for broadband polarization conversion and perfect absorption," IEEE Access. 8, 105815-105823(2020)
12 M. Paquay, J. Iriarte, I. Ederra, R. Gonzalo, P. D Maagt, "Thin AMC structure for radar cross-section reduction," IEEE Trans. Antennas Propag. 55, 3630-3638(2007)
13 C. L. Li, Z. Xu, L. Lin, S. Guo, Y. He, L. Miao, J. J. Jiang, "Ultralow scattering and broadband metasurface using phase adjustable FSS elements embedded with lumped resistors," IEEE Antennas Wireless Propag Lett. 20, 793-797(2021)
14 M. F. El-Sewedy, M. A. Abdalla, "A Monostatic and bistatic RCS reduction using artificial magnetic conductor metasurface," IEEE Trans. Antennas Propag. 71, 1988-1992 (2023)
15 M. Nadi, S. H. Sedighy, M. Khalaj-Amirhosseini, "Ultra wideband radar cross section reduction by using non-resonant unit cells," Sci Rep. 10, 7955 (2020)
16 Y.-J. Zheng, J. Gao, X.-Y. Cao, S.-J. Li, W.-Q. Li, "Wideband RCS reduction and gain enhancement microstrip antenna using chessboard configuration superstrate," Microw. Opt. Technol. Lett. 57, 1738–1741(2015)
17 Y. Zhao, X. Cao, J. Gao, L. Xu, X. Liu and L. Cong, "Broadband low-RCS circularly polarized array using metasurface-based element," IEEE Antennas Wireless Propag Lett. 16, 1836-1839(2017)
18 A. Murugesan, D. Natarajan, K. T. Selvan, "Low-cost, wideband checkerboard metasurfaces for monostatic RCS reduction," IEEE Antennas Wireless Propag Lett. 20, 493-497(2021)

19 W. Chen, C. A. Balanis, C. R. Birtcher, "Checkerboard EBG surfaces for wideband radar cross section reduction," IEEE Trans. Antennas Propag. 63, 2636-2645(2015)
20 W. Chen, C. A. Balanis, C. R. Birtcher, "Dual wide-band checkerboard surfaces for radar cross section reduction," IEEE Trans. Antennas Propag. 64, 4133-4138(2016)
21 A. Y. Modi, C. A. Balanis, C. R. Birtcher, H. N. Shaman, "Novel design of ultrabroadband radar cross section reduction surfaces using artificial magnetic conductors," IEEE Trans. Antennas Propag. 65, 5406–5417(2017)
22 T. Hong, S. Wang, Z. Liu, S. Gong, "RCS reduction and gain enhancement for the circularly polarized array by polarization conversion metasurface coating," IEEE Antennas Wireless Propag Lett. 18, 167-171(2019)
23 C. Fu, Z. Sun, L. Han, C. Liu, "Dual-bandwidth linear polarization converter based on anisotropic metasurface," IEEE Photon. J. 12, 1-11(2020)
24 M. K. T. Al-Nuaimi, W. Hong, Y. He, "Design of diffusive modified chessboard metasurface," IEEE Antennas Wireless Propag Lett. 18, 1621-1625(2019)
25 Y. Lu, J. X. Su, J. B. Liu, Q. X. Guo, H. C. Yin, Z. R. Li, J. M. Song, "Ultrawideband monostatic and bistatic RCS reductions for both copolarization and cross polarization based on polarization conversion and destructive interference," IEEE Trans. Antennas Propag. 67, 4936-4941(2019)
26 J. J. Yang, Y. Z. Cheng, C. C. Ge, R. Z. Gong, "Broadband polarization conversion metasurface based on metal cut-wire structure for radar cross section reduction," Materials. 11, 626, (2018)
27 J. X. Su, Y. Y. Cui, Z. R. Li, Y. Q. Yang, Y. C. Che, H. C. Yin, "Metasurface base on uneven layered fractal elements for ultra-wideband RCS reduction," AIP Adv. 8, 035027 (2018)
28 C. Fu, L. Han, C. Liu, X. Lu, Z. Sun, "Combining Pancharatnam-Berry phase and conformal coding metasurface for dual-band RCS reduction," IEEE Trans. Antennas Propag. 70, 2352-2357(2022)
29 H. Hao, S. Du, T. Zhang, "Small-size broadband coding metasurface for RCS reduction based on particle swarm optimization algorithm," Prog. Electromagn. Res. M. 81, 97-105(2019)
30 S. J. Li, X. Y. Cao, L. M. Xu, L. J. Zhou, H. H. Yang, J. F. Han, Z. Zhang, D. Zhang, X. Liu, C. Zhang, Y. J. Zheng, Y. Zhao, "Ultra-broadband reflective metamaterial with RCS reduction based on polarization convertor, information entropy theory and genetic optimization algorithm," Sci. Rep. 6, 1-12(2016)
31 S. Koziel, M. Abdullah, "Machine-learning-powered EM-based framework for efficient and reliable design of low scattering metasurfaces," IEEE Trans Micro Theory Tech. 69, 2028-2041(2021)
32 MJ. Haji-Ahmadi, V. Nayyeri, M. Soleimani, M. Soleimani, O. M. Ramahi, "Pixelated checkerboard metasurface for ultra-wideband radar cross section reduction," Sci Rep. 7, 11437(2017)
33 Y. Azizi, M. Soleimani, SH. Sedighy, L. Matekovits, "Wideband RCS reduction by single-layer phase gradient modulated surface," Sensors.22, 7108(2022)

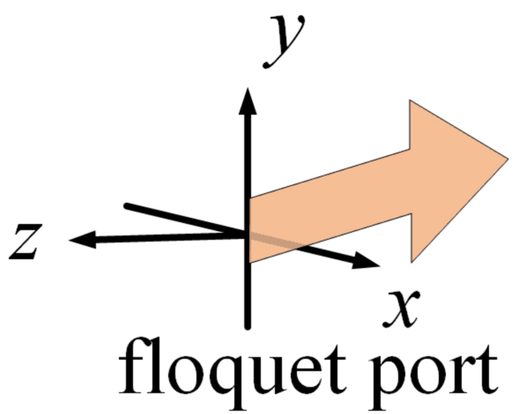

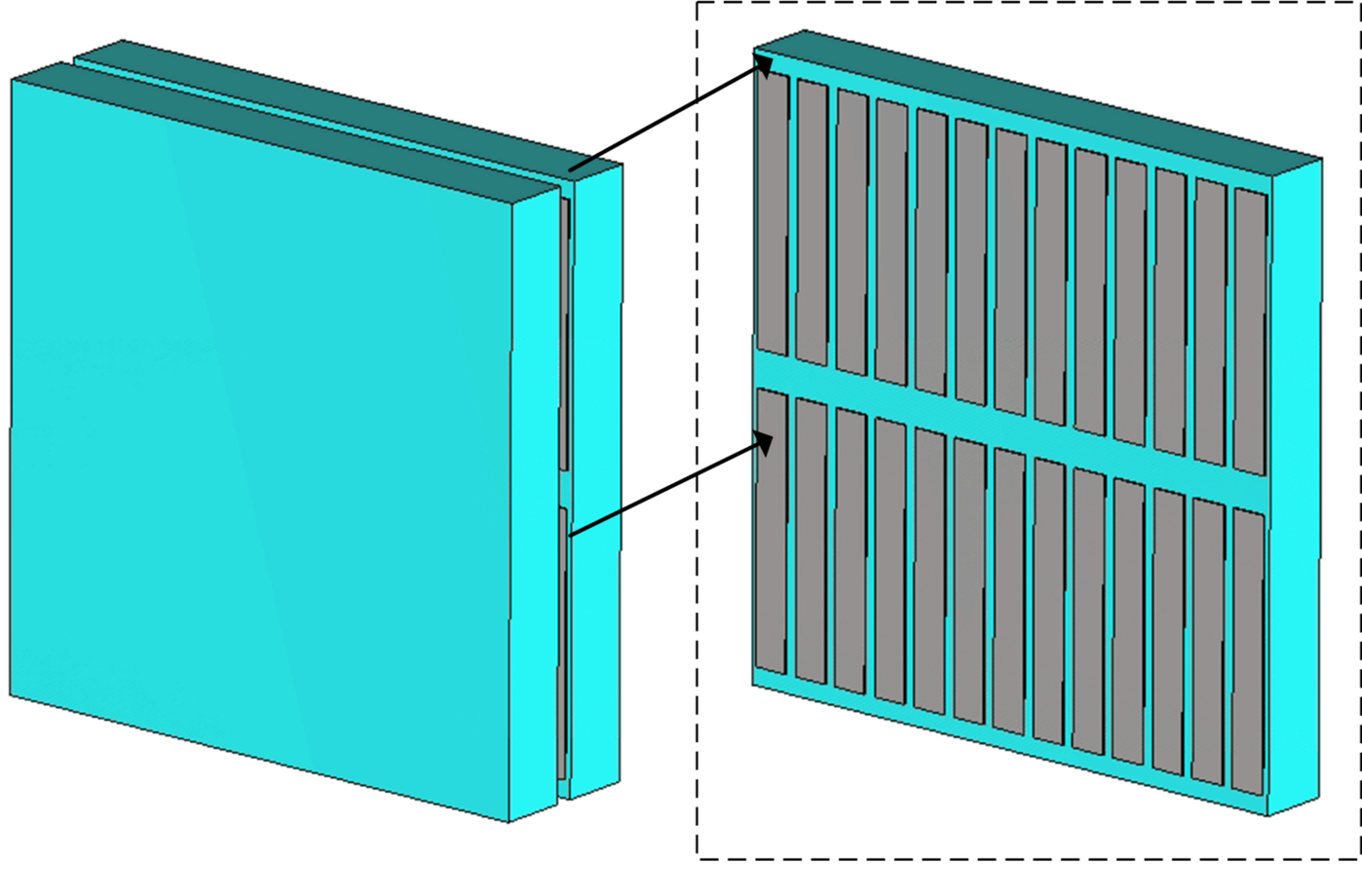

(a)

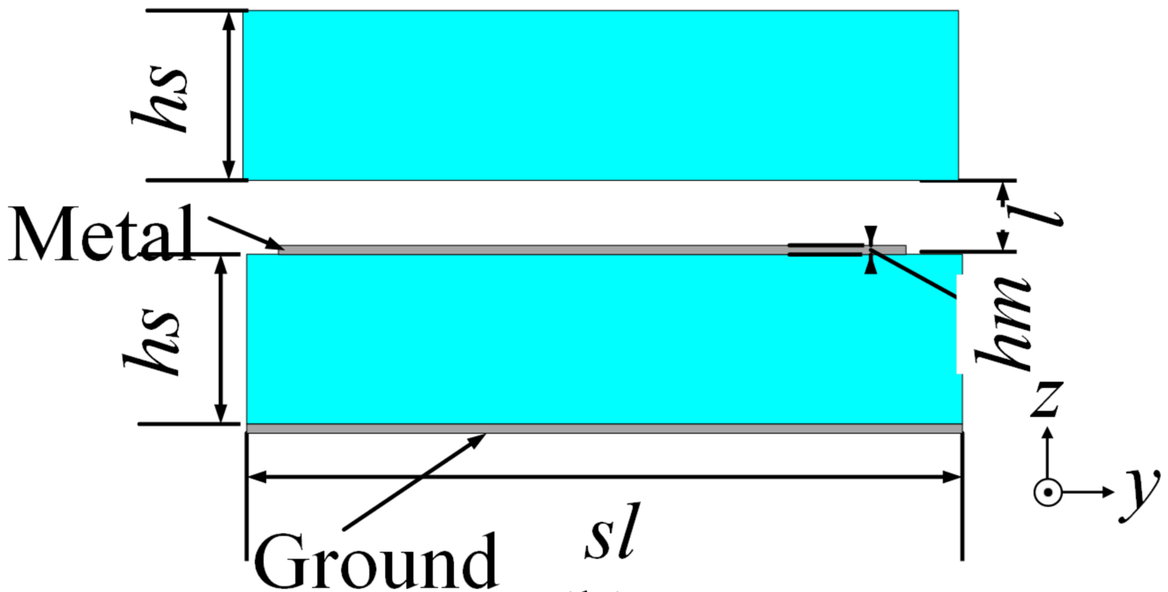

(b)

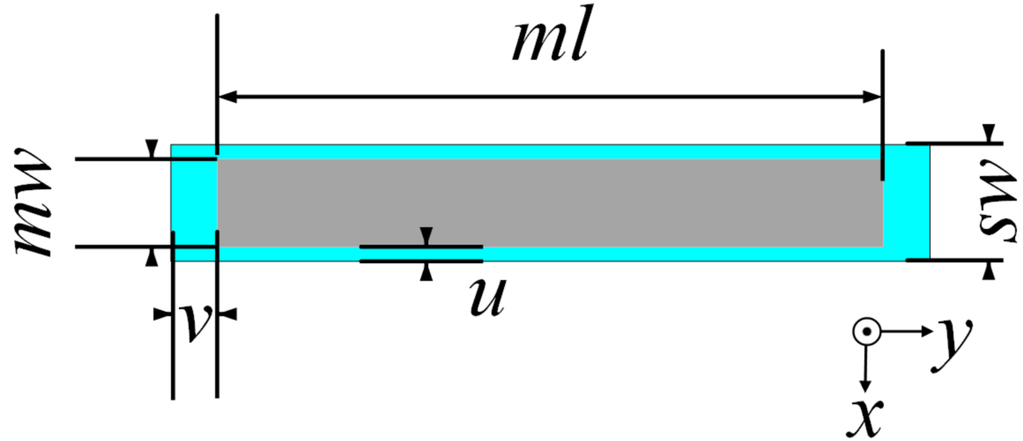

(c)

PLEASE CITE THIS ARTICLE AS DOI: 10.1063/5.0143001

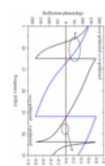

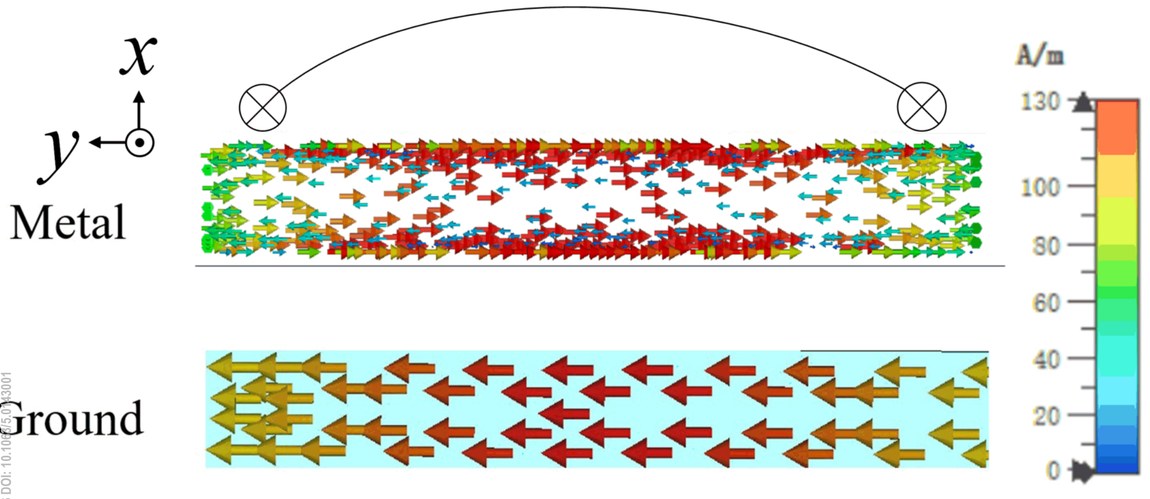

(a)

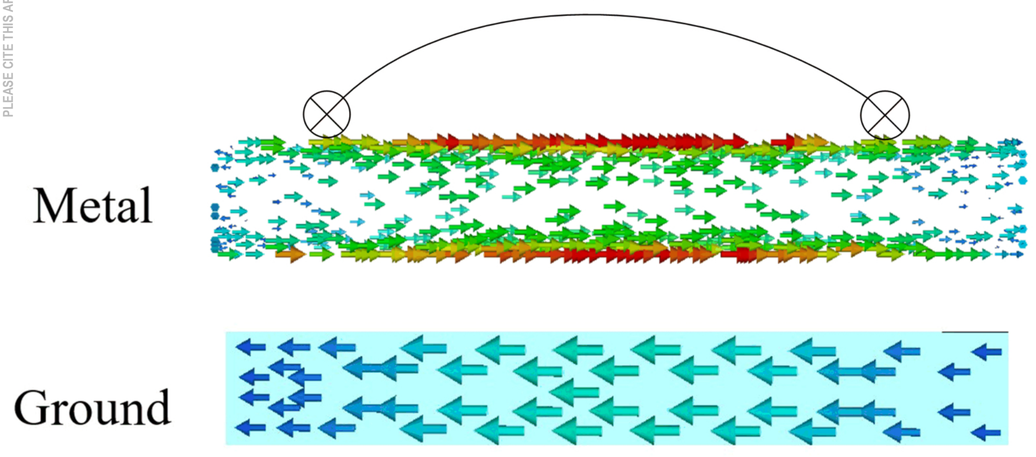

(b)

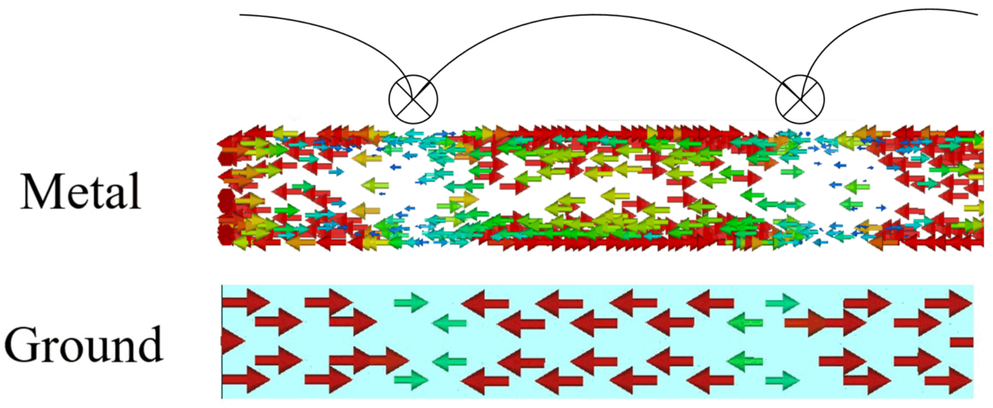

(c)

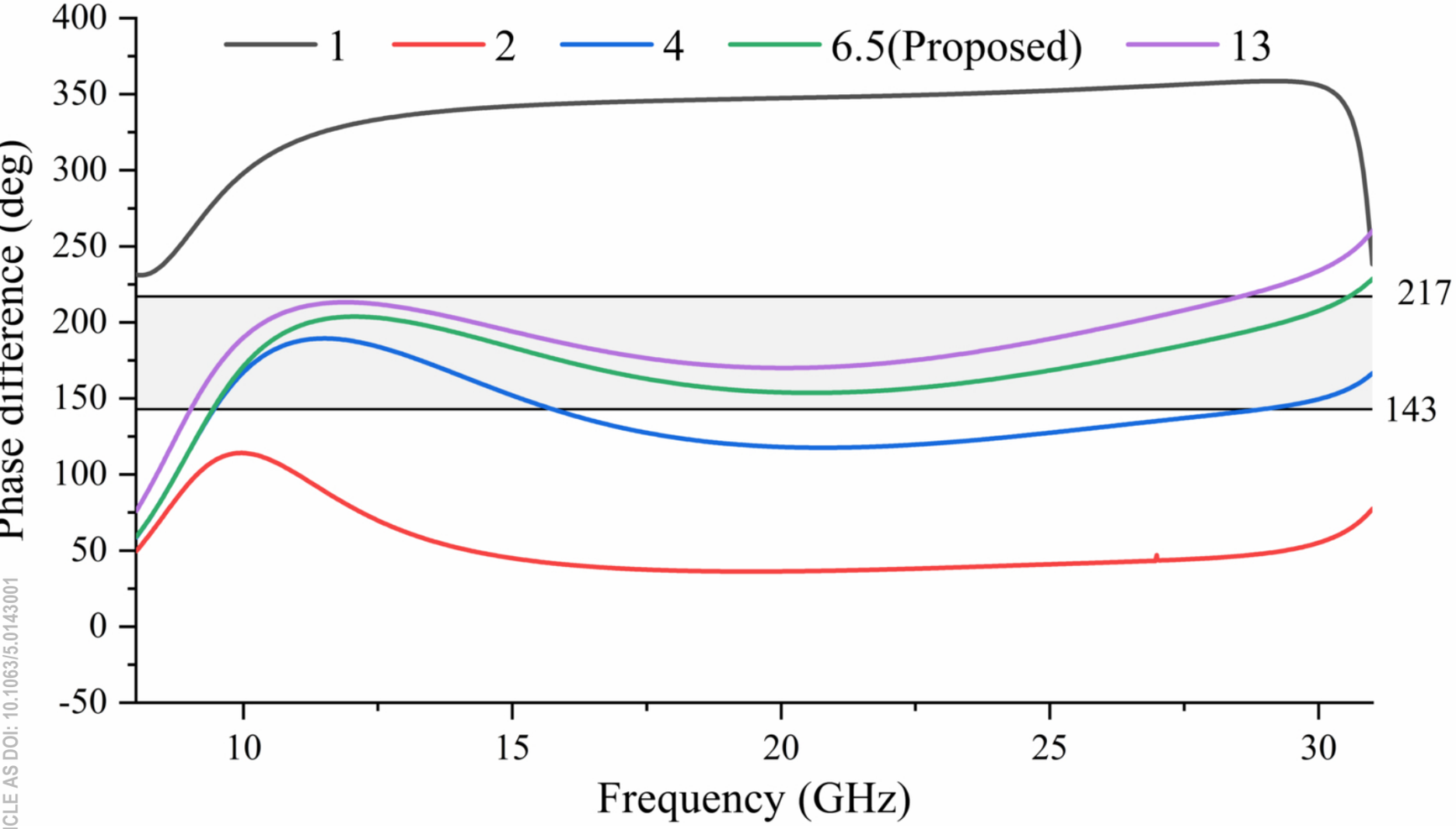

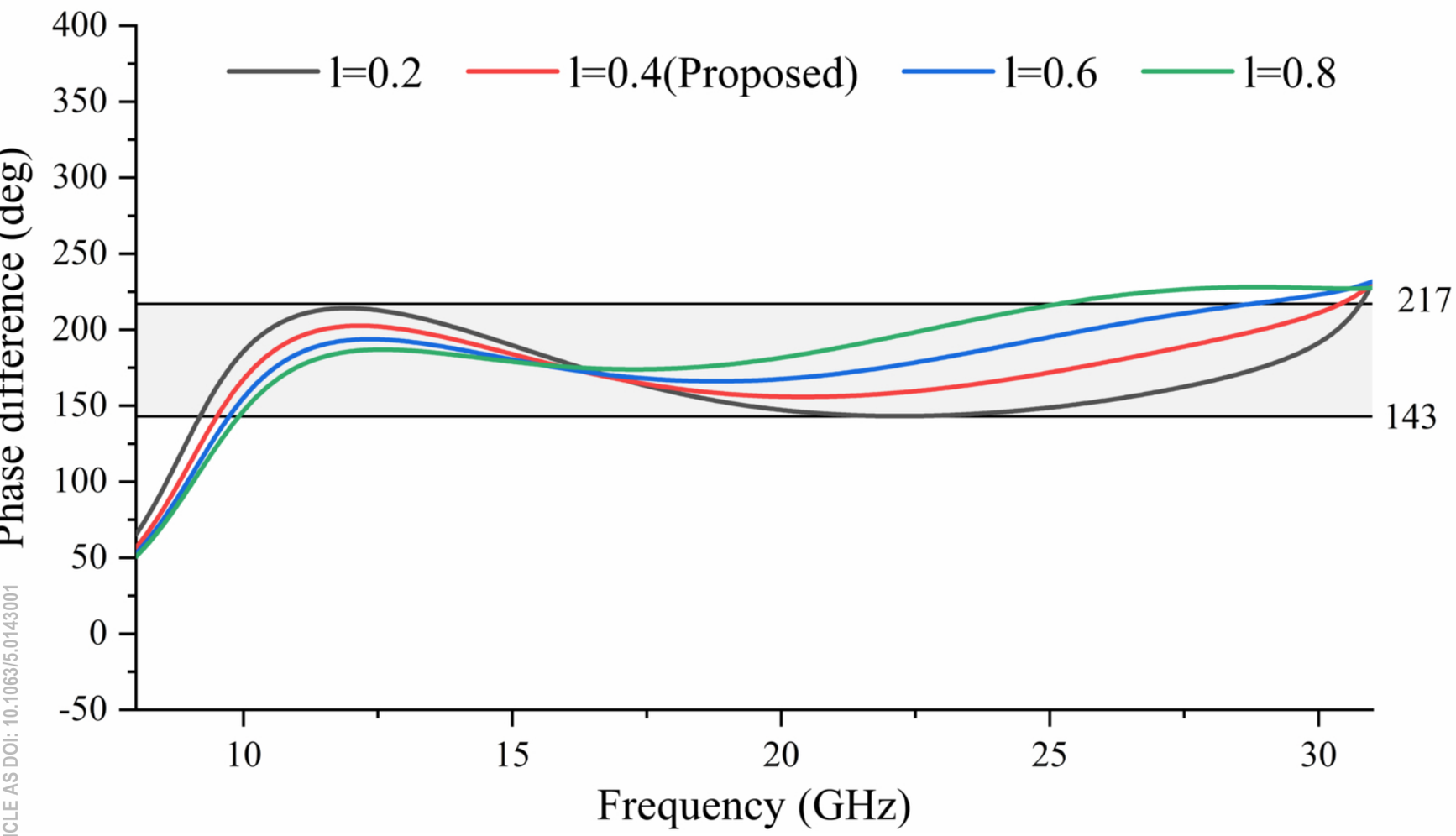

Journal of Applied Physics

AIP Publishing

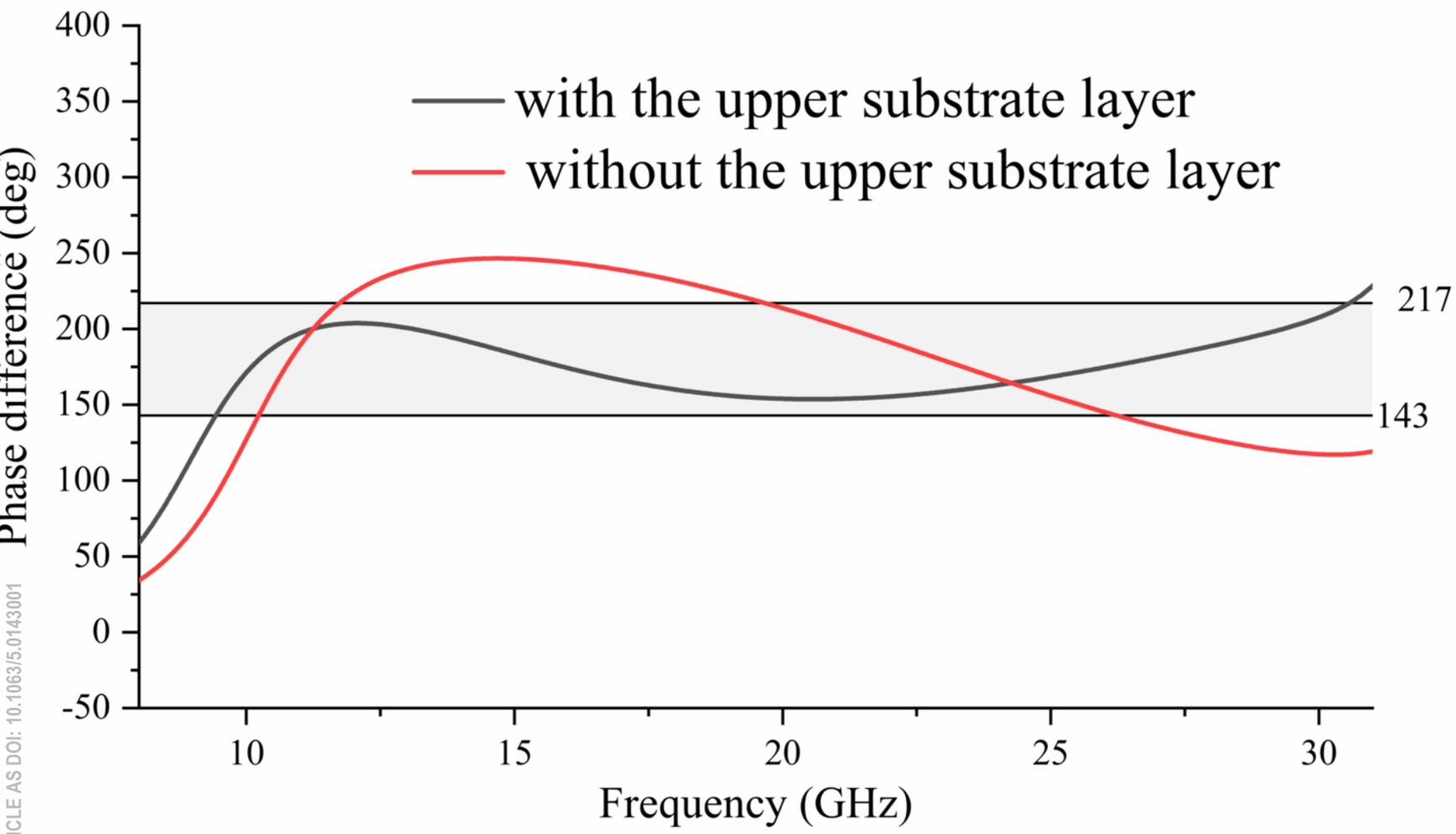

Journal of Applied Physics

AIP Publishing

Journal of Applied Physics

AIP Publishing

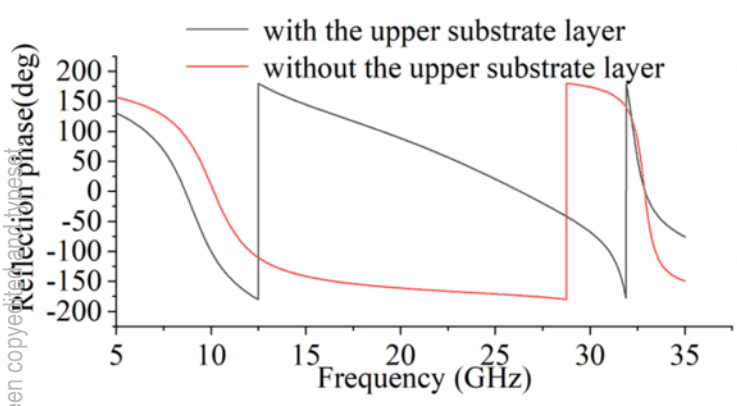

(a)

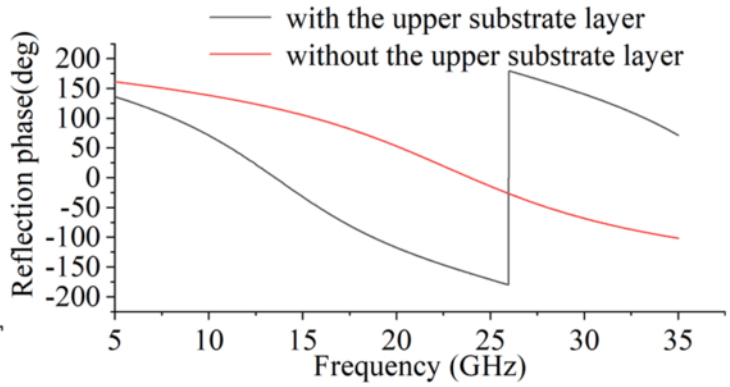

(b)

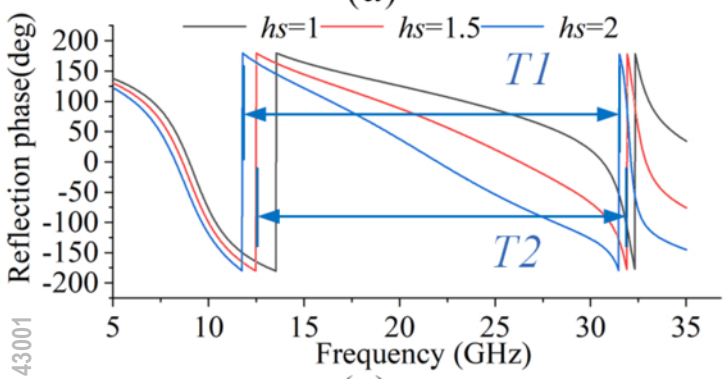

(c)

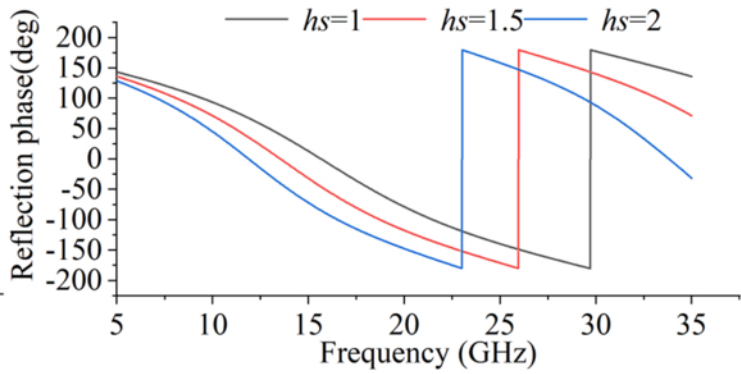

(d)

AIP Publishing

Journal of Applied Physics

ACCEPTED MANUSCRIPT

PLEASE CITE THIS ARTICLE AS DOI: 10.1063/5.0143001

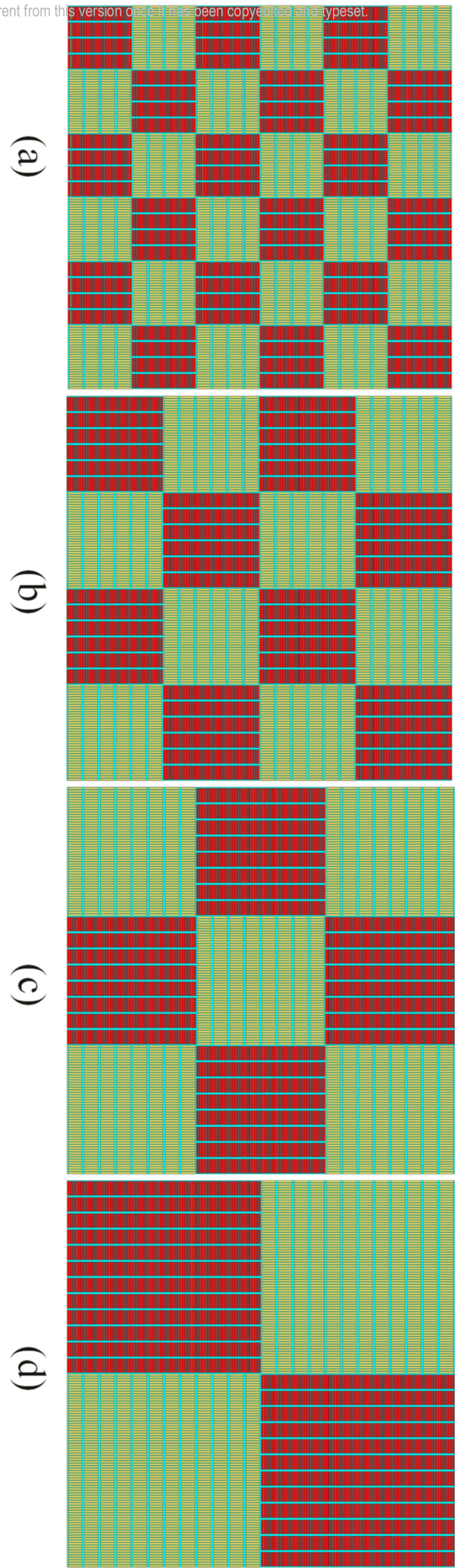

PLEASE CITE THIS ARTICLE AS DOI: 10.1063/5.0143001

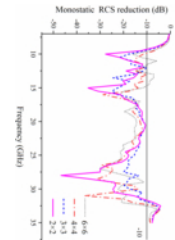

Journal of Applied Physics

AIP Publishing

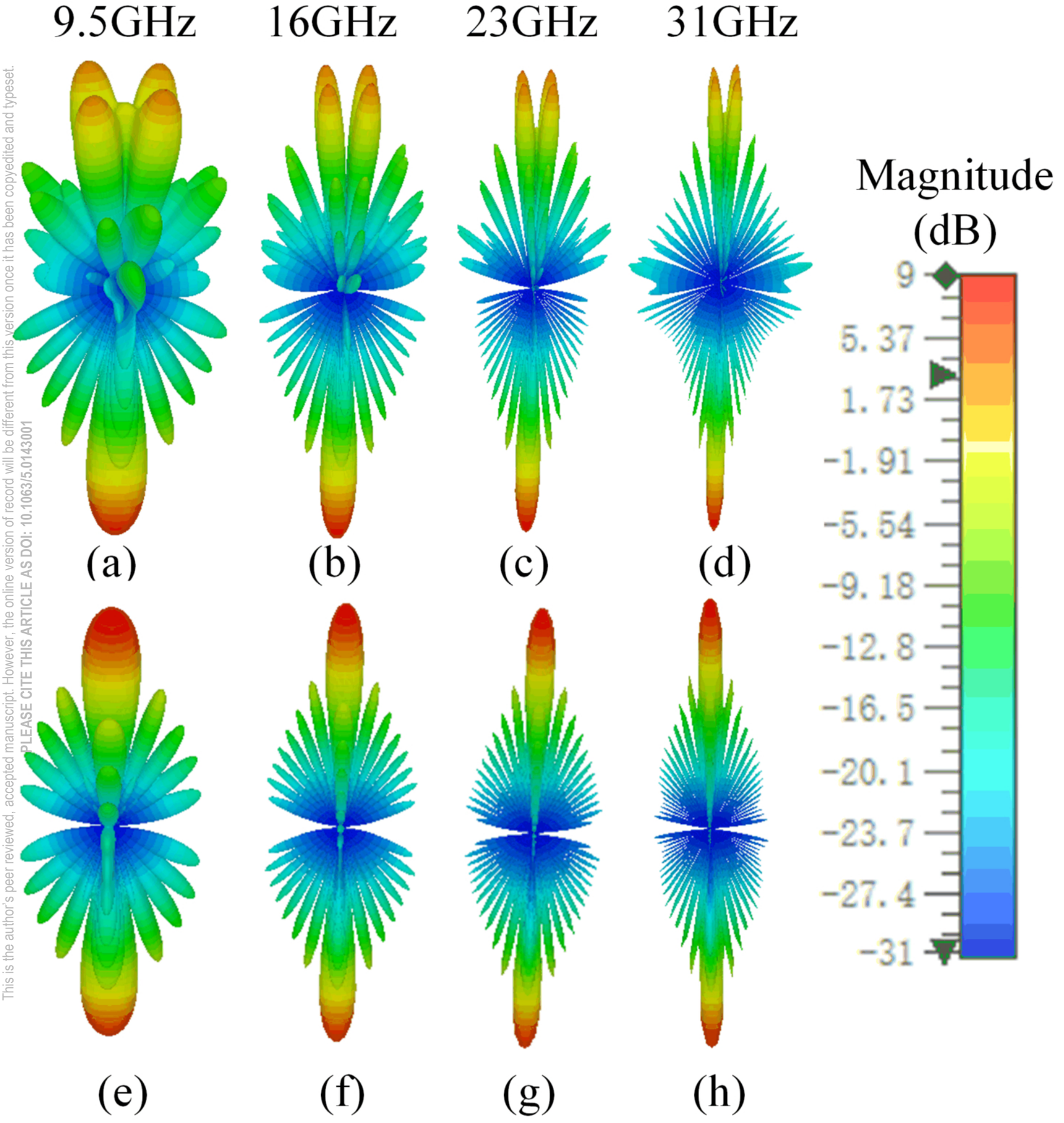

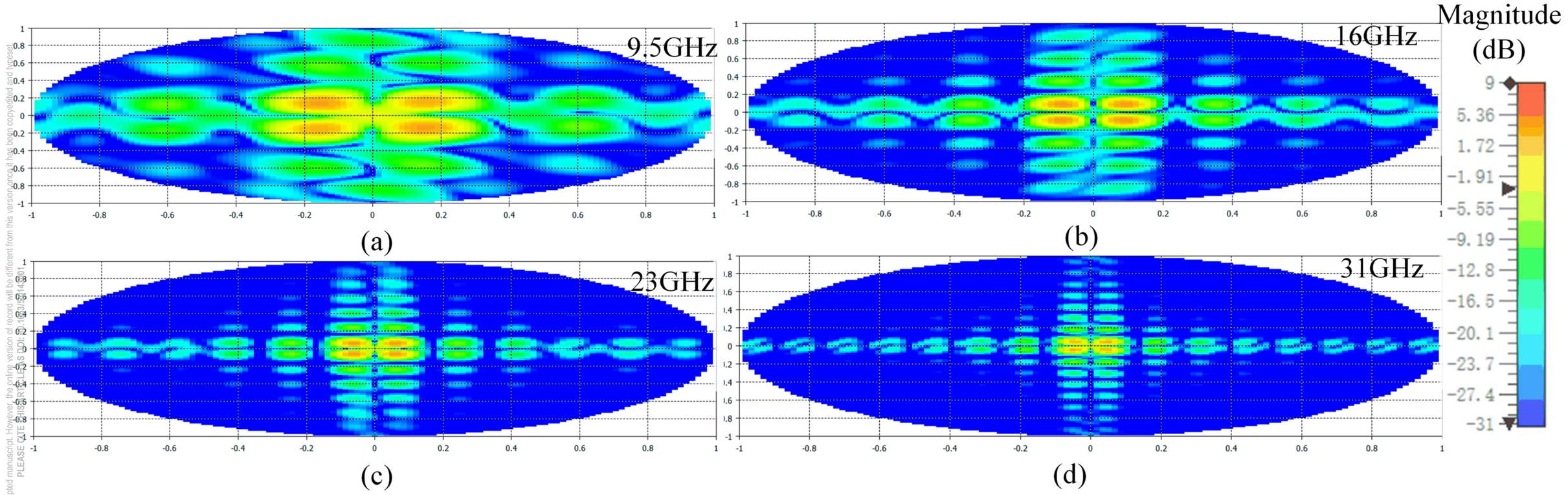

AIP Publishing

Journal of Applied Physics

ACCEPTED MANUSCRIPT

PLEASE CITE THIS ARTICLE AS DOI: 10.1063/5.0143001

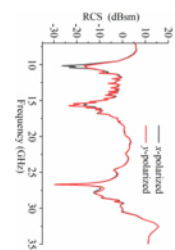

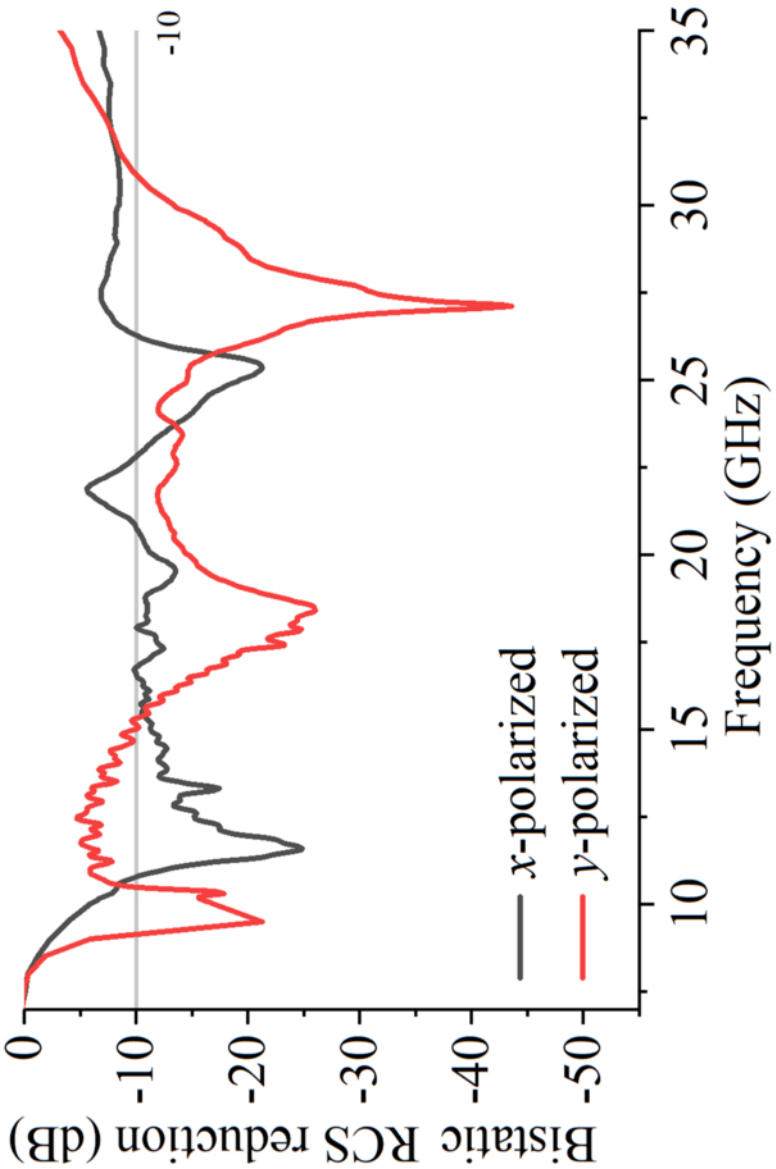

(a)

(b)

Journal of Applied Physics

(a)

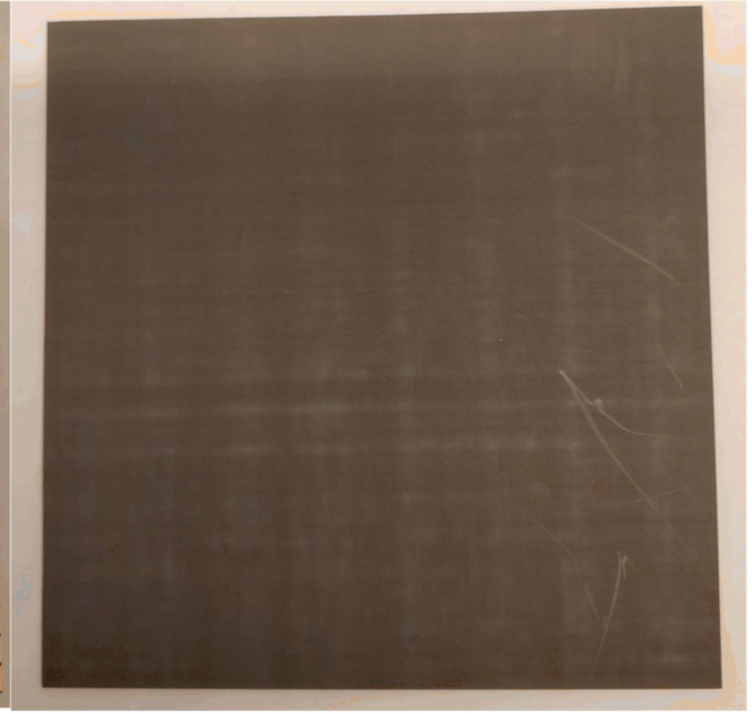

(b)

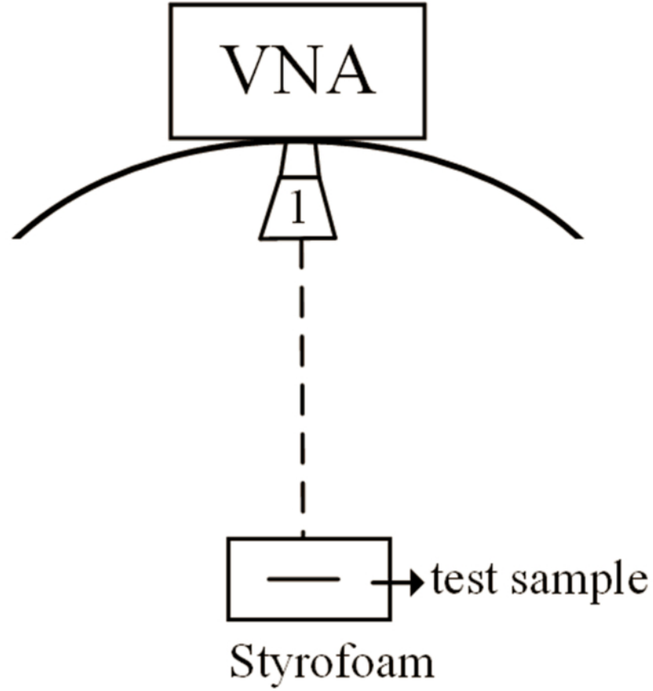

(c)

PLEASE CITE THIS ARTICLE AS DOI: 10.1063/5.0143001